Validating the SAR Wavenumber Shift Principle With the ERS–Envisat PS Coherent Combination

Daniele Perissin, Claudio Prati, Marcus E. Engdahl, and Y. L. Desnos

***Abstract*—Continuity of the European Remote Sensing Satellite Synthetic Aperture Radar (ERS SAR) archive by means of Envisat Advanced SAR (ASAR) data acquired from March 2002 has introduced the problem of the coherent combination of images coming from sensors with slightly different frequencies. The spectral shift principle states that in case of extended distributed targets, the frequency shift is equivalent to a change of looking angle. In this paper, the same principle is exploited to analyze the behavior of permanent scatterers (PSs) with an extension that is smaller than the ground resolution cell. The conditions under which the PSs identified by ERS can be continued by Envisat are then theoretically determined and experimentally validated. Moreover, this analysis shows that acquisitions characterized by different frequencies can be used to identify the slant-range position of scatterers with high subcell accuracy (tens of centimeters). From the processing side, a very precise images coregistration step is required to get the results described in this paper.**

***Index Terms*—Interferometry, synthetic aperture radar (SAR).**

I. Introduction

THE PERMANENT scatterers (PSs) technique is a multiinterferogram algorithm for differential interferometric synthetic aperture radar (DInSAR) analyses developed in the late 1990's to overcome the limits of conventional synthetic aperture radar (SAR) interferometry approaches, namely phase decorrelation and atmospheric effects [1]–[3]. The core purpose of PS analysis is to reconstruct the terrain topography and to monitor deformation phenomena by exploiting long series of SAR data acquired under different geometries and time lags. The accuracy of the height estimate depends on the normal baseline dispersion of the acquisitions [4]. The wider the range of the baselines is, the better the digital elevation model (DEM) estimate is. High values of normal baseline are also a source of decorrelation in correspondence of distributed scatterers [5]; thus, only almost-point-like scatterers are identified because they keep on being coherently imaged.

After the failure of the ERS-2 gyroscope, updating ERS PS measurements by means of the Advanced SAR (ASAR) data became a major issue. Apart from the enhanced ASAR features in terms of acquisition modes and polarimetric capabilities, the main difference between ERS and Envisat ERS-like acquisitions is the carrier frequency (5.3 GHz for ERS-1/2 and 5.331 GHz for Envisat). The 31-MHz frequency shift has a major impact on any interferometric application involving ERS–Envisat data sets because the bandwidth of both systems is less than 18 MHz. ERS–Envisat interferograms usually turn out to be completely decorrelated, at least for typical baseline values (< 1300 m), because no common band is available for distributed targets [5]. Point targets, on the contrary, are expected to remain coherent, and their ERS–Envisat phase histories can be coherently stitched. Moreover, the carrier frequency variation can also be exploited to precisely locate the scatterer in slant range [6]–[8].

Manuscript received October 17, 2005; revised February 23, 2006.

D. Perissin and C. Prati are with the Dipartimento di Elettronica e Informazione, Politecnico di Milano, 20133 Milano, Italy (e-mail: daniele.perissin@polimi.it).

M. E. Engdahl and Y. L. Desnos are with the European Space Agency, European Space Research Institute, 00044 Frascati, Italy.

Digital Object Identifier 10.1109/TGRS.2006.875455

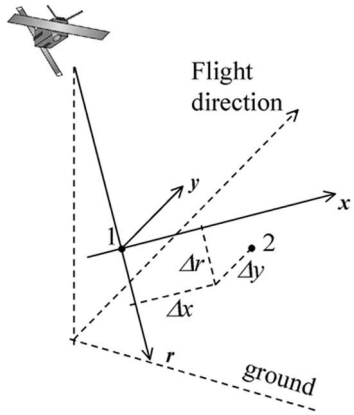

Fig. 1. Radar acquisition geometry of the Master image. r axis: slant-range direction; y axis: flight direction (azimuth); and x axis: normal to the ry plane (cross slant-range direction). 1) First point target, located in the axes origin. 2) Second point target with coordinates Δr, Δx, and Δy.

II. Theoretical Framework

First, the phase stitching theory is considered for point-like targets. Then, the theory will be extended to distributed targets introducing the progressive decorrelation process induced by the scatterers extension.

A. Point-Target Analysis

Let us consider a pair of coregistered SAR images (which will be identified as Master and Slave) and the corresponding interferogram. The data are acquired with a common nominal geometry by two radar systems operating at two slightly different frequencies. Let B_n be the normal baseline (associated to a cross-track angle $\Delta\theta$) and Δf_{DC} the Doppler centroid (DC) frequency difference (associated to an along-track angle $\Delta\psi$) between the Master image, which was acquired at frequency $f_0 - \Delta f$, and the Slave, which was acquired at frequency f_0. In Fig. 1, two nearby point targets 1 and 2 are shown. The

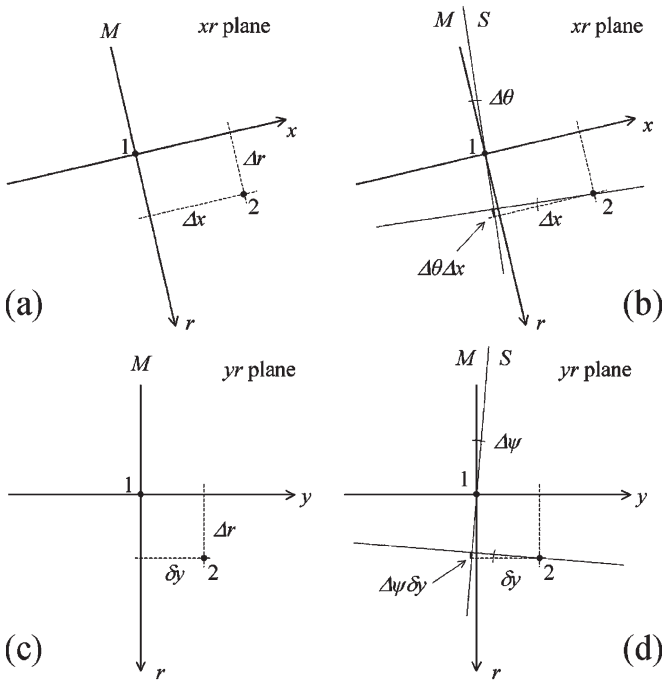

Fig. 2. Master acquisition geometry sections. (a) and (b) xr plane. (c), (d) yr plane. In (b) and (d), the Slave slant-range direction is reported, forming two angles with the Master r axis: (b) $\Delta\theta$ in xr plane and (d) $\Delta\psi$ in yr plane. In (c) and (d), δy is the subpixel azimuth position of target 2, assuming that target 1 is located at the center of the sampling cell.

following orthogonal three-dimensional (3-D) reference system centered at the first point target is then defined:

1) r axis: slant-range direction of the Master image;
2) y axis: flight direction (azimuth) of the Master image;
3) x axis: normal to the ry plane (cross slant-range direction).

In this reference system, the second target has coordinates Δr, Δx, and Δy as shown in Fig. 1.

The following general form of the interferometric phase between the two point targets (1 and 2) holds

$$\Delta\phi_{12} = \phi_{\mathrm{M},12} - \phi_{\mathrm{S},12} \tag{1}$$

where $\phi_{\mathrm{M},12}$ and $\phi_{\mathrm{S},12}$ are the phase differences between the two point targets as seen by the Master and Slave images, respectively. Under the hypothesis of no ground motion and almost no atmospheric phase contribution (close targets [9]), the phase difference $\phi_{\mathrm{M},12}$ only depends on the slant-range distance between the two point targets, which is given as follows:

$$\phi_{\mathrm{M},12} = \frac{4\pi}{c}(f_0 - \Delta f)\Delta r \tag{2}$$

where c is the speed of light. The computation of phase difference $\phi_{\mathrm{S},12}$ has the same form of $\phi_{\mathrm{M},12}$ but for a different frequency (f_0 instead of $f_0 - \Delta f$) and a slightly different slant-range displacement [$\Delta r - \Delta x\Delta\theta - \delta y\Delta\psi$ instead of Δr as shown in Fig. 2(b) and (d)], which is given as follows:

$$\phi_{\mathrm{S},12} = \frac{4\pi}{c} f_0\Delta r - \frac{4\pi}{c} f_0\Delta x\Delta\theta - \frac{4\pi}{c} f_0\delta y\Delta\psi. \tag{3}$$

Here, δy is the subpixel azimuth position of target 2, assuming target 1 is located at the center of the sampling cell.

The interferometric phase can then be expressed as

$$\begin{aligned}\Delta\phi_{12} &= \phi_{\mathrm{M},12} - \phi_{\mathrm{S},12} \\ &= \frac{4\pi}{c}(f_0 - \Delta f)\Delta r - \frac{4\pi}{c} f_0\Delta r \\ &\quad + \frac{4\pi}{c} f_0\Delta x\Delta\theta + \frac{4\pi}{c} f_0\delta y\Delta\psi \\ &= -\frac{4\pi}{c}\Delta f\Delta r + \frac{4\pi}{c} f_0\Delta x\Delta\theta + \frac{4\pi}{c} f_0\delta y\Delta\psi. \end{aligned} \tag{4}$$

In (2.4), besides the two well-known interferometric terms, a new contribution arises. It depends on the frequency difference between Master and Slave and on the slant-range scatterer position. Equation (2.4) highlights the possibility of locating in the 3-D space a target by means of SAR interferometry.

Equation (2.4) can be rewritten as a function of the normal baseline B_n and of the DC frequency difference Δf_{DC}. Defining R_0 the sensor distance from the origin, the incidence angle difference is $\Delta\theta = B_n/R_0$. Starting from [10], we have the following relation between the squint angle ψ and the DC frequency f_{DC}

$$f_{\mathrm{DC}} = -\frac{2v}{c} f_0 \sin\psi \tag{5}$$

where v is the sensor velocity, and $\psi = \psi_0 + \Delta\psi$ is the Slave squint angle. Computing the difference with respect to the Master acquisition characterized by a squint angle ψ_0 (whose typical value is very close to 0), we obtain

$$\Delta f_{\mathrm{DC}} = \frac{2v}{c} f_0\Delta\psi\cos\psi_0 \simeq \frac{2v}{c} f_0\Delta\psi \tag{6}$$

and introducing the azimuth sampling step δ_{az} and the pulse repetition frequency PRF, we have

$$\Delta\psi = \frac{c}{2\delta_{\mathrm{az}}\mathrm{PRF} f_0}\Delta f_{\mathrm{DC}}. \tag{7}$$

Equation (2.4) can thus be rewritten as

$$\Delta\phi_{12} = -\frac{4\pi}{c}\Delta f\Delta r + \frac{4\pi f_0 B_n}{cR_0}\Delta x + 2\pi\frac{\Delta f_{\mathrm{DC}}}{\mathrm{PRF}}\frac{\delta y}{\delta_{\mathrm{az}}}. \tag{8}$$

In the framework of a multiinterferogram analysis, like the PS technique, the three terms in (8) can be separated by exploiting their different behaviors in the parameter space Δf, B_n, Δf_{DC}, and the three coordinates Δr, Δx, and δy can be estimated. In case of an ERS–Envisat data set, only two different frequencies are present and thus a single value for Δf. Consequently, the first term in (8) is different from point to point but constant in all ERS–Envisat interferograms. This term shall be referred to as the location phase screen (LPS) in the following. Given the 31-MHz frequency shift, the LPS changes by almost two cycles across a single slant-range resolution cell (giving an LPS ambiguity of about 5 m), thus, it is extremely sensitive to the target slant-range position within the resolution cell.

The variance of the slant-range position estimated from the LPS exploiting N ERS images and M Envisat images can be

expressed from the first term in (8) as a function of the phase dispersion in the different acquisitions and is given by

$$\sigma^2_{\Delta r} = \left(\frac{c}{4\pi\Delta f}\right)^2 \left(\frac{\sigma^2_{\Delta\phi_{\rm ERS}}}{N} + \frac{\sigma^2_{\Delta\phi_{\rm Envisat}}}{M}\right). \quad (9)$$

According to (9), with $N = 60$ and $M = 10$, a PS with multiinterferogram coherence $\gamma = 0.8$ ($\gamma = e^{-\sigma^2_{\Delta\phi}/2}$ [3]) can be positioned with uncertainty of about 20 cm.

The LPS can be connected to the slant-range scatterer position estimated through the peak of the radar return amplitudes. A PS with a given radar cross section RCS can be positioned in slant range, from N archived ERS SAR images, with the following uncertainty (see the Appendix):

$$\sigma_{\Delta r} \approx \frac{\rho_{\rm rg}}{\sqrt{3N}}\sqrt{\frac{\sigma_0 A_{\rm c}}{\rm RCS}} \quad (10)$$

where σ_0 is the backscattering coefficient of the clutter surrounding the PS, $A_{\rm c}$ is the area of the ERS resolution cell, and $\rho_{\rm rg}$ is the ERS slant-range resolution. In case of urban areas and ERS typical values ($RCS = 500$ m^2, $A_{\rm c} = 125$ m^2, $\sigma_0 = 0$ dB, $N = 60$, and $\rho_{\rm rg} = 9$ m), we get $\sigma_{\Delta r} \simeq 30$ cm, which is comparable with what was obtained from the LPS.

B. Impact of the Physical Extension of the Target

Let us consider the same interferogram described at the beginning of the previous section. Whereas pointwise targets are seen coherently by definition in both images, a distributed scatterer may lose coherence when observed under a different acquisition geometry. To quantify the phenomenon, we derive the expression of the target coherence as a function of the frequency shift Δf, the incidence angle difference $\Delta\theta$, and the squint angle variation $\Delta\psi$ between the two images. The coherence is obtained as the absolute value of the normalized cross-correlation coefficient between the Master image $S_{\rm M}$ and the Slave $S_{\rm S}$. The coherence has the usual well-known form [11], but in this case, it depends also on a frequency change, i.e.,

$$\gamma(\Delta f, \Delta\theta, \Delta\psi) = \left|\frac{E\left[S_{\rm M}S^*_{\rm S}\right]}{\sqrt{E\left[|S_{\rm M}|^2\right]E\left[|S_{\rm S}|^2\right]}}\right|. \quad (11)$$

The distributed target is modeled under the first-order Born approximation as the sum of a high number of elementary point targets with no mutual interaction on an absorbing background. The complex reflectivity value s of the elementary point scatterers is described as independent identically distributed zero-mean complex Gaussian variate that is fully defined by its variance σ^2. For the sake of simplicity, we analyze a single distributed target formed by many elementary point scatterers uniformly distributed into a cubic box with sides L_r, L_x, and L_y in slant range, cross slant range, and azimuth, respectively (Fig. 3).

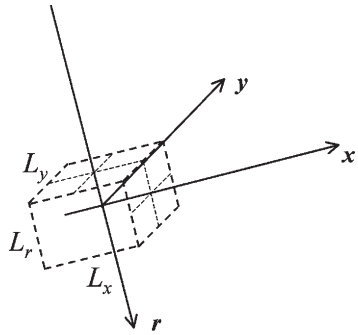

Fig. 3. Distributed scatterer model in the Master acquisition geometry. The target is formed by many elementary point targets uniformly distributed into a cubic box with sides L_r, L_x, and L_y in slant range, cross slant range, and azimuth, respectively.

The pixel complex value of the Master image $S_{\rm M}$ in correspondence to the distributed target can be approximated as the sum of the elementary reflectivities, which is expressed as

$$S_{\rm M} \simeq \int_{-\frac{L_r}{2}}^{\frac{L_r}{2}}\int_{-\frac{L_x}{2}}^{\frac{L_x}{2}}\int_{-\frac{L_y}{2}}^{\frac{L_y}{2}} s(r,x,y)e^{-j\frac{4\pi}{c}(f_0-\Delta f)r_{\rm M}}drdxdy \quad (12)$$

where $r_{\rm M} = R_0 + r$ is the distance between the sensor and the scatterers, which is localized by the coordinates r, x, and y.

Here, the onboard filters (both in time/slant range and azimuth) weights have been assumed constant along the resolution cell to keep mathematics as simple as possible. Such an approximation does not change so much the final result because we assume that the distributed target extension is smaller than the resolution cell.

Similarly, for the Slave, we have

$$S_{\rm S} \simeq \int_{-\frac{L_r}{2}}^{\frac{L_r}{2}}\int_{-\frac{L_x}{2}}^{\frac{L_x}{2}}\int_{-\frac{L_y}{2}}^{\frac{L_y}{2}} s(r,x,y)e^{-j\frac{4\pi}{c}f_0 r_{\rm S}}drdxdy \quad (13)$$

where the sensor-targets distance $r_{\rm S} = R_0 + r - x\Delta\theta - y\Delta\psi$ takes into account the different geometries.

The expected value of the cross-correlation coefficient can be calculated, observing that all cross-products between different scatterers are zero for the reflectivity independency, by

$$\begin{aligned} E[S_{\rm M}S^*_{\rm S}] \simeq & E\left[\int_{-\frac{L_r}{2}}^{\frac{L_r}{2}}\int_{-\frac{L_x}{2}}^{\frac{L_x}{2}}\int_{-\frac{L_y}{2}}^{\frac{L_y}{2}} s(r,x,y)e^{-j\frac{4\pi}{c}(f_0-\Delta f)r_{\rm M}}drdxdy\ldots\right. \\ & \left.\int_{-\frac{L_r}{2}}^{\frac{L_r}{2}}\int_{-\frac{L_x}{2}}^{\frac{L_x}{2}}\int_{-\frac{L_y}{2}}^{\frac{L_y}{2}} s^*(r',x',y')e^{j\frac{4\pi}{c}f_0 r_{\rm S}}dr'dx'dy'\right] \\ = & \sigma^2 e^{j\frac{4\pi}{c}\Delta f R_0} \\ & \times E\left[\int_{-\frac{L_r}{2}}^{\frac{L_r}{2}}\int_{-\frac{L_x}{2}}^{\frac{L_x}{2}}\int_{-\frac{L_y}{2}}^{\frac{L_y}{2}} e^{-j\frac{4\pi}{c}(-r\Delta f + f_0 x\Delta\theta + f_0 y\Delta\psi)}drdxdy\right]. \end{aligned} \quad (14)$$

Recalling the Fourier transform of a rectangle

$$\int_{-\frac{\Delta}{2}}^{\frac{\Delta}{2}} e^{-j2\pi\xi\tau}d\tau = \Delta\frac{\sin(\pi\Delta\xi)}{\pi\Delta\xi} \tag{15}$$

and taking the normalized absolute value of (14), the coherence expression (11) becomes

$$\gamma(\Delta f, \Delta\theta, \Delta\psi) \simeq \left|\frac{\sin\left(\pi L_r \frac{2\Delta f}{c}\right)}{\pi L_r \frac{2\Delta f}{c}}\frac{\sin\left(\pi L_x \frac{2f_0\Delta\theta}{c}\right)}{\pi L_x \frac{2f_0\Delta\theta}{c}}\frac{\sin\left(\pi L_y \frac{2f_0\Delta\psi}{c}\right)}{\pi L_y \frac{2f_0\Delta\psi}{c}}\right|. \tag{16}$$

Exploiting the relations found in the previous section, we can write the coherence as a function of frequency shift Δf, normal baseline B_n, and DC frequency difference $\Delta f_{\rm DC}$, i.e.,

$$\gamma(\Delta f, B_n, \Delta f_{\rm DC}) \simeq \left|\frac{\sin\left(\pi L_r \frac{2\Delta f}{c}\right)}{\pi L_r \frac{2\Delta f}{c}}\frac{\sin\left(\pi L_x \frac{2f_0 B_n}{cR_0}\right)}{\pi L_x \frac{2f_0 B_n}{cR_0}}\frac{\sin\left(\pi L_y \frac{\Delta f_{\rm DC}}{\delta_{\rm az}\rm PRF}\right)}{\pi L_y \frac{\Delta f_{\rm DC}}{\delta_{\rm az}\rm PRF}}\right|. \tag{17}$$

Equation (17) sums up in a simple form the complex phenomenon of geometrical decorrelation in the 3-D space. A pointwise target ($L_r = L_x = L_y = 0$) is not affected by geometrical decorrelation ($\gamma = 1$) even for high values of Δf, B_n, and $\Delta f_{\rm DC}$. A target with finite dimensions on the contrary is coherently observed only under a limited range of view angles. If the view angles overcome such limits, the target progressively loses coherence. On the other hand, given the distribution of acquisition parameters (Δf, B_n, and $\Delta f_{\rm DC}$), a target must be smaller than a critical threshold to be coherently seen by the sensor. The theoretical maximum size of a scatterer can be easily obtained by calculating the values of L_r, L_x, and L_y, making the argument of the cardinal sines equal to 1 ($\gamma = 0$). For ERS typical values (central frequency $f_0 = 5.3$ GHz and closest approach distance $R_0 \simeq 830$ km), we obtain numbers well known in SAR interferometry (index c means critical)

$$L_{x\rm c} = \frac{cR_0}{2f_0 B_{nc}} \simeq 20 \text{ m with } B_{nc} \simeq 1300 \text{ m} \tag{18}$$

$$L_{y\rm c} = \frac{\delta_{\rm az}\rm PRF}{\Delta f_{\rm DCc}} \simeq 4 \text{ m with } \frac{\Delta f_{\rm DCc}}{\rm PRF} = 1. \tag{19}$$

For the ERS–Envisat coherent combination, the 31 MHz of frequency gap leads to

$$L_{r\rm c} = \frac{c}{2\Delta f} \simeq 5 \text{ m with } \Delta f = 31 \text{ MHz}. \tag{20}$$

If ERS stable scatterers were perfectly pointwise, we should expect to observe them coherently also under the ERS–Envisat frequency shift (100% of survival rate). For targets distributed in a volume, loss of coherence, and consequently, lower ERS–Envisat PS's survival rate is expected.

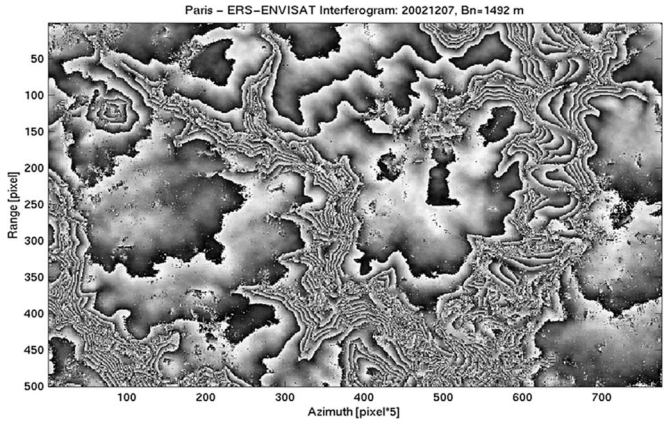

Fig. 4. ERS–Envisat interferogram on a rural area including the rivers Reveillon and Yerres near Paris characterized by a normal baseline of 1500 m and a temporal baseline of 30 min. High coherence is found even in vegetated areas of the interferogram.

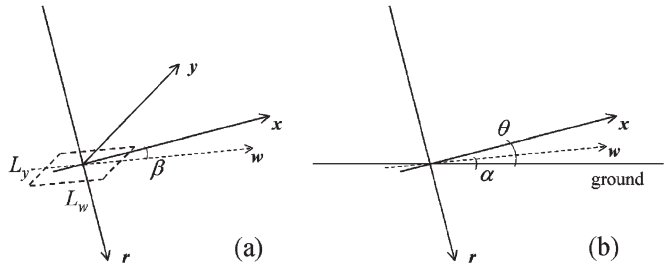

Fig. 5. Surface scattering model in the Master acquisition geometry. (a) Target of extensions L_y and L_w lies on the yw plane; the β angle is between the w axis and x axis. (b) Angle β can be expressed as a function of the incidence angle θ and the target inclination with respect to the ground α: $\beta = \theta - \alpha$.

Fig. 4 shows an ERS–Envisat interferogram on a rural area including the rivers Reveillon and Yerres near Paris characterized by a normal baseline of 1500 m. It is worth noting that the ERS–Envisat interferogram in Fig. 4 shows high coherence even in vegetated areas. This example suggests that the main scattering mechanism in the C-band cannot be volumetric. In fact, as stated in (17), a volume target distribution would have generated much lower coherence. The solution has to be found in a different scattering mechanism. In the following subsection, we analyze the impact of a carrier frequency shift on distributed surface targets.

C. Wavenumber Shift Principle

The case of flat surface scattering is a degeneration of volumetric scattering and deserves a separate analysis. The assumptions for the target model are the same as described for the cubic case at the beginning of the previous subsection, but the elementary scatterers are uniformly distributed on a planar surface of extensions L_y and L_w as shown in Fig. 5(a). The target lies on the yw plane, where the w axis is rotated of an angle α from the horizontal [Fig. 5(b)].

The expression of the coherence (11) as a function of the acquisition geometry can be computed as previously done, taking into account the surface target distribution. The pixel complex value of Master and Slave images are obtained as the

double integral of the complex reflectivity along the directions w and y, i.e.,

$$S_{\mathrm{M}} \simeq \int_{-\frac{L_w}{2}}^{\frac{L_w}{2}} \int_{-\frac{L_y}{2}}^{\frac{L_y}{2}} s(w,y) e^{-j\frac{4\pi}{c}(f_0-\Delta f)(R_0+r)} dw dy \tag{21}$$

$$S_{\mathrm{S}} \simeq \int_{-\frac{L_w}{2}}^{\frac{L_w}{2}} \int_{-\frac{L_y}{2}}^{\frac{L_y}{2}} s(w,y) e^{-j\frac{4\pi}{c} f_0(R_0+r-x\Delta\theta-y\Delta\psi)} dw dy. \tag{22}$$

The r and x coordinates have to be expressed as a function of the coordinate w. Posing $\beta = \theta - \alpha$ (Fig. 5), we have $r = w\sin\beta$ and $x = w\cos\beta$. Thus, the cross-correlation coefficient between the Master image S_{M} and the Slave S_{S} becomes

$$E\left[S_{\mathrm{M}} S_{\mathrm{S}}^*\right] \simeq \sigma^2 e^{j\frac{4\pi}{c}\Delta f R_0} \times E\left[\int_{-\frac{L_w}{2}}^{\frac{L_w}{2}} \int_{\frac{L_y}{2}}^{\frac{L_y}{2}} e^{-j\frac{4\pi}{c}(-w\sin\beta\Delta f + f_0 w\cos\beta\Delta\theta + f_0 y\Delta\psi)} dw dy\right]. \tag{23}$$

Following the same computational steps described previously, we obtain the following expression of the coherence of a surface scatterer:

$$\gamma(\Delta f, B_n, \Delta f_{\mathrm{DC}}) \simeq \left| \frac{\sin\left[\frac{2\pi L_w}{c}\left(f_0\frac{B_n}{R_0}\cos\beta - \Delta f\sin\beta\right)\right]}{\frac{2\pi L_w}{c}\left(f_0\frac{B_n}{R_0}\cos\beta - \Delta f\sin\beta\right)} \times \frac{\sin\left(\pi L_y \frac{\Delta f_{\mathrm{DC}}}{\delta_{\mathrm{az}}\mathrm{PRF}}\right)}{\pi L_y \frac{\Delta f_{\mathrm{DC}}}{\delta_{\mathrm{az}}\mathrm{PRF}}} \right|. \tag{24}$$

Equation (24) is the product between a cardinal sine that depends on the target azimuth dimension L_y (already seen in the volume scattering case) and a new cardinal sine relative to the second dimension L_w. The argument of the new cardinal sine in (24) shows that there is a particular baseline that compensates for the frequency shift (the spectral shift principle [5]): $f_0(B_n/R_0)\cos\beta - \Delta f\sin\beta = 0$. In this case, the scatterer extension does not introduce any decorrelation. The baseline B_n that compensates for a frequency shift Δf is a function of the target slope α and incidence angle θ, i.e.,

$$B_n = \frac{\Delta f}{f_0} R_0 \tan(\theta - \alpha). \tag{25}$$

In case of the ERS–Envisat frequency gap, the compensation baseline for flat horizontal terrain is about 2 km, which is very close to the baseline value of the interferogram in Fig. 4. Thus, surface scattering is at the origin of the high interferogram coherence in Fig. 4. Equation (24) is an alternative formulation of the wavenumber shift principle [5] where the target size has been left variable.

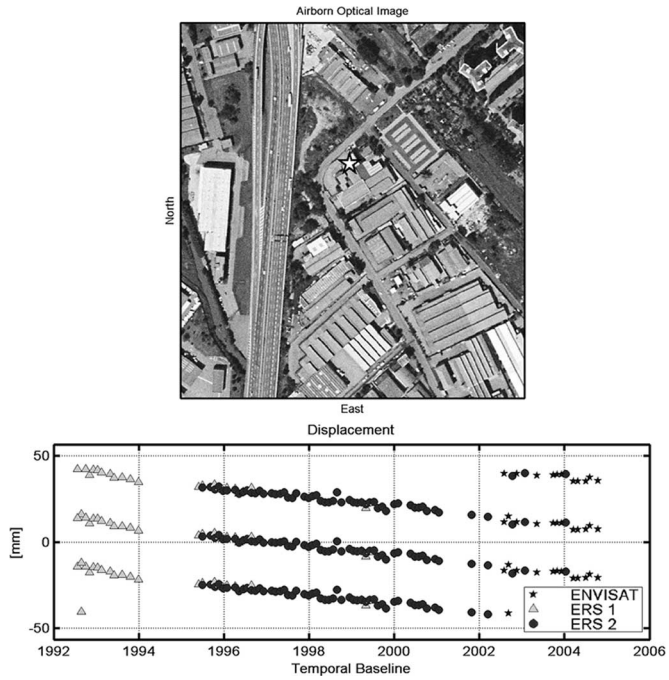

Fig. 6. PS example. (Top) The PS location in Milan is identified with a white star on an airborne optical image. (Bottom) PS time series. Each marker of the series refers to a displacement measure derived from ERS-1 (triangles), ERS-2 (dots), and Envisat (stars) at the date indicated on the abscissa. Two adjacent replica ($\pm$28 mm) are plotted to eliminate ambiguities.

III. Experimental Results

To assess the theoretical framework discussed in the previous sections, we carried out a PS analysis on a SAR data set including 82 ERS and 12 Envisat images acquired over Milan, Italy (Track 208, Frame 2691). The test area covers about 400 km^2. The ERS image acquired on January 14, 1997 is selected as the master scene, and all the slave acquisitions (ERS and Envisat) are resampled on the common master grid, taking into account the different PRFs and sampling frequencies in the range direction.

The PS processing follows the description reported in [1], i.e., adopting a two-step strategy. First, PS candidates (PSCs) are selected by means of the amplitude stability index [1]. For each PSC, four phase terms dependent on the relative elevation, the Doppler differences, the frequency shift, and a possible constant relative velocity are jointly estimated. Phase residuals should then depend only on atmospheric effects, noise, and possible phase components due to the nonuniform motion of the targets. The atmospheric phase screen (APS) of each interferogram is estimated from the phase residuals exploiting its statistical behavior [12] and is then removed from the data. Finally, PSs are detected on a pixel-by-pixel basis [1]. The multiinteferogram coherence [3] of each PS is computed on the ERS and Envisat data sets separately to estimate their survival rate when the radar operating frequency changes. In Fig. 6, an example of time series is shown, together with the georeferenced position of the scatterer on an aerial photo.

A. ERS–Envisat Continuity

In Table I, the main results of the coherence analysis and PS survival rate are reported. The number of PSs having ERS

TABLE I
SURVIVAL RATE FOR DIFFERENT COHERENCES. FOR EACH THRESHOLD VALUE (FIRST COLUMN), NUMBER OF POINTS WITH ERS COHERENCE ($N = 82$ IMAGES) GREATER THAN THE THRESHOLD (SECOND COLUMN) AND NUMBER OF POINTS WITH BOTH ERS AND ENVISAT ($M = 12$ IMAGES) COHERENCE GREATER THAN THE THRESHOLD (THIRD COLUMN) ARE GIVEN. FOURTH COLUMN: PERCENT RATIO

Coherence	ERS	ERS & Envisat	%
0.70	46200	28500	62
0.80	32000	17700	55
0.85	23000	12000	52
0.90	12700	6400	50
0.95	2900	1300	45

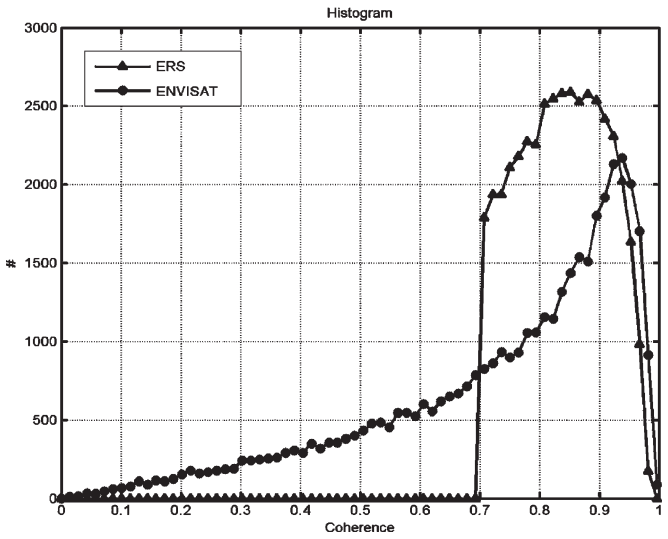

Fig. 7. ERS (triangles) and Envisat (dots) PS coherence histograms of the analyzed points.

coherence (estimated on 82 ERS images) greater than the value indicated in the first column is reported in the second column. The third column reports the number of PSs showing coherence greater than that indicated in the first column on both ERS (82 images) and Envisat (12 images) time series. The PS survival rate is shown in the last column of Table I as the percent ratio between the second and third columns, and it tells the percentage of PSs that maintain the coherence over a certain threshold passing from ERS to Envisat. More than 60% of PSs with ERS coherence greater than 0.7 have the same stability in Envisat data, whereas by increasing the threshold to 0.95, the percentage becomes about 40%.

The accuracy of the estimate of the multiinterferogram coherence is inversely proportional to the number of images [3]. The Envisat coherence is thus less accurate than the one calculated in ERS acquisitions. Notwithstanding, the PS survival rate can be considered reliable, because it is estimated as the ratio of a high number of points.

A more detailed analysis of the PS's survival rate is shown in Fig. 7. Here, the ERS coherence histogram (triangles) of PSs showing coherence greater than 0.7 is compared with the Envisat coherence histogram (dots) of the same PSs.

In Fig. 8, we show the density of points of the scatter plot between the estimated LPS in radians (y axis) and the slant-range position of the analyzed PSs expressed in meters (x axis).

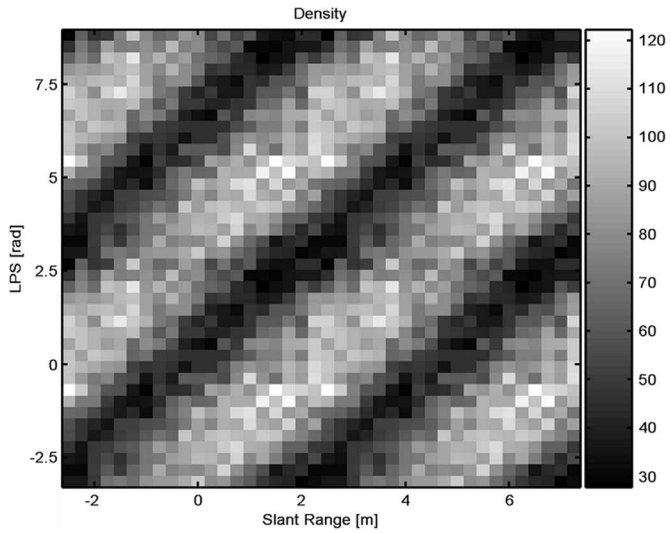

Fig. 8. Density of points of the scatter plot between the ERS–Envisat LPS (in radians) (y axis) and the PS position (in meters) (x axis) extracted from the peak of the reflectivity map. For visualization purposes, the scatter plot has been replicated both on the vertical (2π) and horizontal axes (5 m). Grayscale indicates the data density.

The PS slant-range position has been obtained by extracting the peak of the reflectivity map (i.e., the incoherent time average of the images; see the Appendix) in correspondence of the PS. As seen in the previous section [see the first term of (8)], the LPS depends linearly on the scatterer slant-range location with a 2π phase ambiguity corresponding to 5 m of slant-range ambiguity. For visualization purposes, the scatter plot has been replicated both on the vertical (2π) and horizontal (5 m) axes. The good correlation found (dispersion about 1 m) is a proof of the location capability of the PS technique.

B. Validation of the Wavenumber Shift Principle

The results on the survival of PSs when passing from ERS to Envisat data can be used for validating the wavenumber shift principle. As seen in Section II-C, the spectral shift principle states an equivalence between a carrier frequency slight change and a variation of the normal baseline (i.e., the off-nadir angle). This equivalence leads to the expression of the normal baseline that compensates for the ERS–Envisat frequency gap $\Delta f = 31$ MHz (25). The compensation baseline for flat horizontal terrain is about 2 km (note that, here, the baseline is derived with respect to the master acquisition, and therefore, it has a sign and can be negative). This means that at the compensation baseline, Envisat observes a distributed scatterer as it would have been observed by ERS at zero baseline. In this framework, when the ERS orbit is assumed as a reference, it is useful to introduce an *equivalent Envisat baseline*, which is shifted by -2 km with respect to its actual value, accounting for the ERS–Envisat frequency shift.

The amplitude of the radar returns of the ERS images as a function of the view angle (normal baseline) corresponds to a portion of the backscattering radiation pattern of the radar target at 5.3 GHz (the ERS operating frequency). Following the spectral shift principle, the amplitude of the radar returns of the Envisat images should then correspond to a part of the PS radiation pattern shifted by -2 km on the ERS baseline

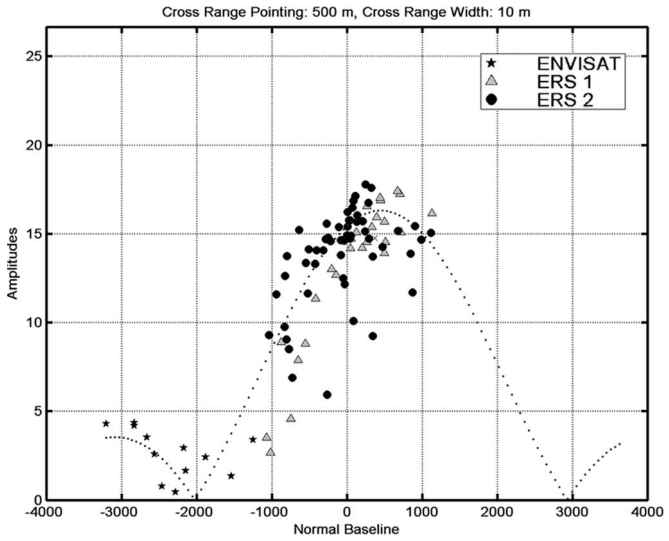

Fig. 9. Amplitudes versus baseline (in meters). ERS-1 (triangles), ERS-2 (dots), and Envisat (stars) data relative to a PS. Envisat data are shifted by -2 km, which compensates for the frequency shift. (Dashed line) Cardinal sine fitting the data. Envisat values fall close to zero.

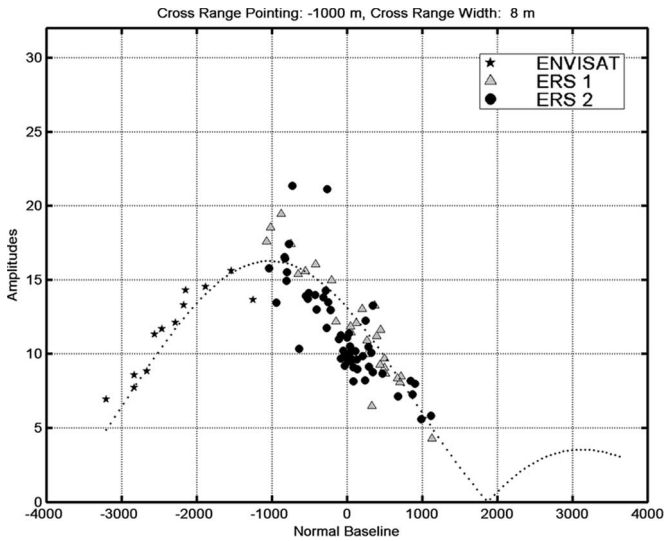

Fig. 10. Amplitudes versus baseline (in meters). ERS-1 (triangles), ERS-2 (dots), and Envisat (stars) data relative to a PS. Envisat data are shifted by -2 km, which compensates for the frequency shift. (Dashed line) Cardinal sine fitting the data. Envisat values fall around the maximum.

axis. In Figs. 9 and 10, two examples of the PS amplitudes as a function of the baseline are shown. In case of the Envisat data, the equivalent baseline (shifted by -2 km) is used. It should be noted how the ERS PS radiation pattern is consistently continued by the Envisat measurements.

The portion of the radiation pattern illuminated by Envisat can be connected to the PS multiinterferogram coherence in the Envisat data. In fact, whenever the PS radiation pattern seen by Envisat is close to zero (as in Fig. 9), the Envisat PS phase coherence is low. On the other hand, if Envisat looks around a local maximum (as in Fig. 10), Envisat data show high coherence.

In Fig. 11, we show this behavior on the whole set of PSs analyzed. Assuming, for the sake of simplicity, that the PS can be modeled as a mirror, its radiation pattern as a function of the looking angle can be approximated with a cardinal sine. The

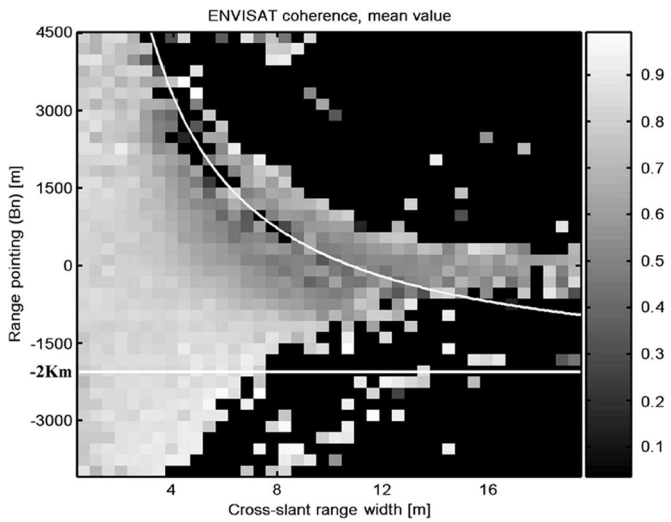

Fig. 11. Envisat coherence dependency on the target geometry (width and pointing). (x axis) Cross slant-range scatterer width (in meters). (y axis) Cross slant-range pointing (in meters) (amplitudes mainlobe peak position along baseline). Grayscale: Envisat coherence mean value. The data plotted are ERS PSs ($\gamma_{\mathrm{ERS}} > 0.7$). White line: theoretical (3.1) PS geometry (width and pointing) that generates a first zero of the scattering pattern in -2 km.

width of the cardinal sine is therefore inversely proportional to the spatial extension of the PS, whereas the portion of the radiation pattern illuminated by the radar gives information on its orientation. In Fig. 11, the x axis represents the target cross slant-range width L_x (which is inversely proportional to the cardinal sine mainlobe width) estimated from the ERS data set. The y axis is the target orientation (i.e., the cardinal sine mainlobe position on the baseline axis, expressed in meters) again estimated from the ERS data set. The zero baseline corresponds to the ERS Master acquisition, which is chosen for minimizing the dispersion of the baselines. The grayscale in Fig. 11 shows the average coherence estimated from Envisat data only on the PS set identified by the ERS data with $\gamma_{\mathrm{ERS}} > 0.7$. Black areas in Fig. 11 (zero coherence) show a lack of ERS PSs with such width and pointing.

The actual baselines of the Envisat images cluster around the same ERS zero reference baseline. However, for a simpler analysis of this key figure, it is useful to imagine that they cluster around the equivalent reference baseline located at -2 km, accounting for the ERS–Envisat frequency shift.

Point scatterers have a constant radiation pattern, and the cardinal sine model assigns a zero width to them. They do not need a particular orientation to be seen by the satellite. In Fig. 11, they appear uniformly distributed along the whole range of baselines, and they also have high coherence in Envisat data despite the frequency shift.

When the estimated cross slant-range width increases, the target must be pointed toward the master ERS acquisition to be identified as an ERS PS. This theoretically predicted behavior for distributed targets is confirmed by the experimental data in Fig. 11, where ERS PS distribution shrinks around the zero baseline for higher values of the cross slant-range width.

Moreover, a darker (low Envisat coherence) curved area is clearly visible in Fig. 11 going from the upper left to the middle right of the grayscale image. This interesting feature deserves a detailed analysis because it represents the experimental validation of spectral shift principle applied to SAR missions with

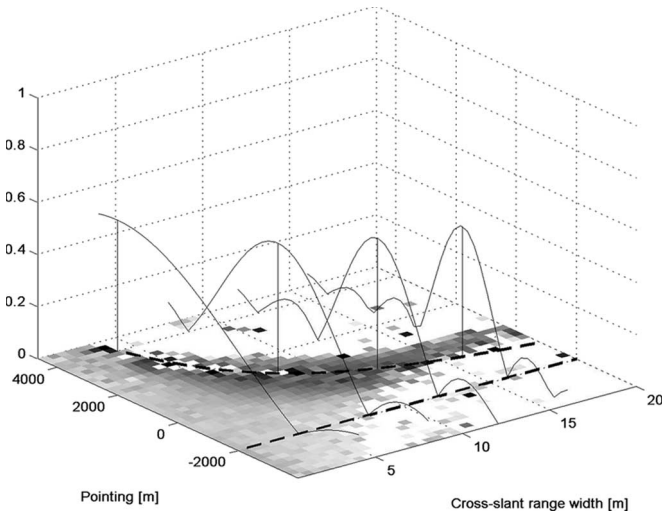

Fig. 12. Scattering pattern examples of targets with a geometry (width and pointing) that generates a first zero in -2 km. Theoretical width and pointing of scattering patterns with a zero in -2 km lie on the black dashed line (26).

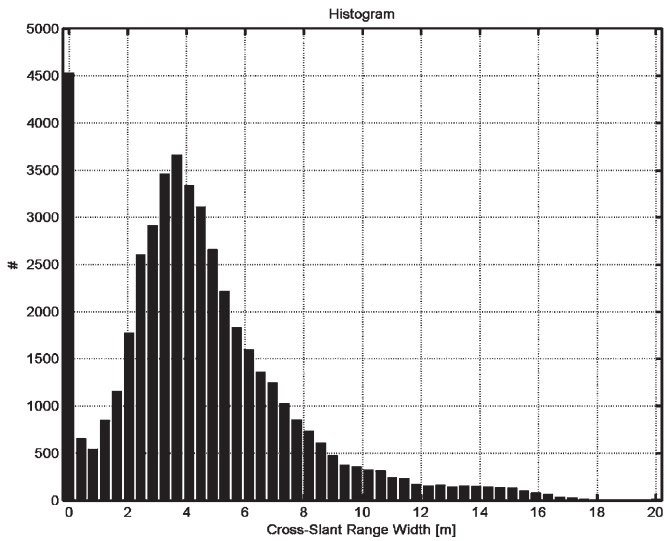

Fig. 13. Histogram of the estimated cross slant-range widths of the analyzed PSs ($\gamma_{\rm ERS} > 0.7$).

slightly different carrier frequencies. Let us consider a class of PSs whose width L_x estimated from the ERS data set is, say, 8 m. The Envisat average coherence of this class of PSs is represented by the gray level of the small square pixels aligned along a column in Fig. 11. The vertical coordinate shows the estimated pointing angle (which is expressed as the normal baseline with respect to the reference ERS orbit) of the strongest target backscattering (i.e., the angular orientation of peak of the cardinal sine backscattering pattern). As already pointed out, the actual Envisat orbits cluster along the same ERS reference orbit (namely the baseline 0 in Fig. 11); however, they should be shifted by -2 km to take into account the frequency shift with respect to ERS. Thus, high Envisat coherence is expected from targets with their strongest backscattering located around -2 km, whereas low coherence is expected from targets whose backscattering radiation pattern shows a zero at -2 km. The first zero of the backscattering pattern is obtained by

$$B_{n,\rm zero} = \frac{cR_0}{2f_0}\frac{1}{L_x}. \tag{26}$$

Getting back to our example, for an $L_x = 8$ m width target, the first zero is at about 3000 m. In our theoretical model, a low Envisat coherence value is thus expected at those pixels located along the 8-m-wide column in Fig. 11 about 3000 m above -2 km. The same can be done for every target width as visualized in Fig. 12, thus identifying the curve (white in Fig. 11 and black dashed in Fig. 12) where low Envisat coherence is expected. The experimental data of Figs. 11 and 12 clearly validate the theoretical model.

In Fig. 13, the histogram of the estimated cross slant-range widths of the analyzed PSs ($\gamma_{\rm ERS} > 0.7$) is reported. The amplitude analysis shows that less than 20% of PSs can be considered as point scatterers (the estimated cross slant-range width is less than 50 cm). The other urban radar targets are more complex objects that behave as distributed, even if with widths that do not fill the resolution cell. Their Envisat coherence can thus be predicted in first approximation by looking at the portion of their reflectivity at the Envisat frequency. The study on the electromagnetic characteristics of SAR urban targets deserves much more analysis, which will be covered in another paper.

IV. Conclusion

In this paper, we have presented the theory of coherent stitching of PS phase histories detected by ERS and Envisat characterized by slightly different carrier frequencies. The results obtained over Milan combining 82 ERS and 12 Envisat images with the PS technique validate the theory and demonstrate that the ESA ERS C-band archive can be continued with the new Envisat acquisitions. Envisat ASAR can be usefully exploited to continue the displacement time series of more than 60% of ERS SAR PSs, despite the frequency gap between the two radars. It has been shown that a single PS data set can be formed using ERS and Envisat images with a common ERS master image. Moreover, the joint analysis of ERS and Envisat surveys adds new insight on the physical nature of the PS.

Appendix

The PS slant-range position can be extracted from the peak of the radar return amplitudes. The problem can be simplified as the estimate of the peak of a cardinal sine in the presence of additive white Gaussian noise. For the sake of simplicity, we take a normalized cardinal sine centered around the origin as

$$S(r) = \frac{\sin\frac{\pi r}{\rho_{\rm rg}}}{\frac{\pi r}{\rho_{\rm rg}}} + n \tag{A1}$$

where $\rho_{\rm rg}$ is the system range resolution and n is the white Gaussian noise with variance σ_n^2.

The peak is identified by the zero of the first derivative. Exploiting the Taylor series expansion of second order, the cardinal sine around the origin is approximated as

$$\frac{\sin\frac{\pi r}{\rho_{\rm rg}}}{\frac{\pi r}{\rho_{\rm rg}}} \simeq 1 - \frac{\pi^2 r^2}{6\rho_{\rm rg}^2} \tag{A2}$$

and thus

$$S'(r) \simeq -\frac{\pi^2 r}{3\rho_{\mathrm{rg}}^2} + n'. \tag{A3}$$

The solution is found posing $S'(r) = 0$, i.e.,

$$r = \frac{3\rho_{\mathrm{rg}}^2}{\pi^2} n'. \tag{A4}$$

We are interested in the dispersion of the location estimate defined by

$$\sigma_r^2 = \left(\frac{3\rho_{\mathrm{rg}}^2}{\pi^2}\right)^2 E\left[(n')^2\right] \tag{A5}$$

and, thus, we need to calculate the power of the noise derivative as follows:

$$\begin{aligned} E[(n')^2] &= \int_{-\frac{1}{2\rho_{\mathrm{rg}}}}^{\frac{1}{2\rho_{\mathrm{rg}}}} S_{n'(k_r)dk_r} \\ &= \int_{-\frac{1}{2\rho_{\mathrm{rg}}}}^{\frac{1}{2\rho_{\mathrm{rg}}}} \sigma_n^2 |j2\pi k_r|^2 dk_r \\ &= \frac{\pi^2 \sigma_n^2}{3\rho_{\mathrm{rg}}^2}. \end{aligned} \tag{A6}$$

Substituting (A6) in (A5), we obtain

$$\sigma_r^2 = \frac{3\rho_{\mathrm{rg}}^2}{\pi^2}\sigma_n^2. \tag{A7}$$

Because we took a normalized radar response, the noise power can be expressed as the noise-to-signal ratio defined by

$$\sigma_n^2 = \frac{\sigma_0 A_{\mathrm{c}}}{\mathrm{RCS}} \tag{A8}$$

where σ_0 is the backscattering coefficient of the clutter surrounding the PS, A_{c} is the area of the ERS resolution cell, and RCS is the PS radar cross section. Exploiting N archived SAR images, the slant-range scatterer position uncertainty is then given as follows:

$$\sigma_r \approx \frac{\rho_{\mathrm{rg}}}{\sqrt{3N}} \sqrt{\frac{\sigma_0 A_{\mathrm{c}}}{\mathrm{RCS}}}. \tag{A9}$$

ACKNOWLEDGMENT

The authors would like to thank ESA for the Envisat and ERS data (provided under ESRIN Contract 16564/02/I-LG) as well as the whole Tele-Rilevamento Europa staff for processing ERS and Envisat images.

REFERENCES

[1] A. Ferretti, C. Prati, and F. Rocca, "Permanent scatterers in SAR interferometry," *IEEE Trans. Geosci. Remote Sens.*, vol. 39, no. 1, pp. 8–20, Jan. 2001.

[2] ——, "Non-linear subsidence rate estimation using permanent scatterers in differential SAR interferometry," *IEEE Trans. Geosci. Remote Sens.*, vol. 38, no. 5, pp. 2202–2212, Sep. 2000.

[3] C. Colesanti, A. Ferretti, F. Novali, C. Prati, and F. Rocca, "SAR monitoring of progressive and seasonal ground deformation using the permanent scatterers technique," *IEEE Trans. Geosci. Remote Sens.*, vol. 41, no. 7, pp. 1685–1701, Jul. 2003.

[4] A. Ferretti, C. Prati, and F. Rocca, "Requirements for a space mission for DInSAR and PS analysis based on past and present missions," in *Proc. IGARSS*, 2004, vol. 3, pp. 1695–1698.

[5] F. Gatelli *et al.*, "The wavenumber shift in SAR interferometry," *IEEE Trans. Geosci. Remote Sens.*, vol. 32, no. 4, pp. 855–865, Jul. 1994.

[6] C. Colesanti, A. Ferretti, D. Perissin, C. Prati, and F. Rocca, "ERS–Envisat permanent scatterers interferometry," in *Proc. IGARSS*, 2004, vol. 2, pp. 1130–1132.

[7] A. Ferretti, D. Perissin, C. Prati, and F. Rocca, "ERS–Envisat permanent scatterers," in *Proc. IGARSS*, 2004, vol. 2, pp. 985–988.

[8] M. Arrigoni, C. Colesanti, A. Ferretti, D. Perissin, C. Prati, and F. Rocca, "Identification of the location phase screen of ERS–Envisat permanent scatterers," in *Proc. FRINGE*, Frascati, Italy, Dec. 1–5, 2003. ESA SP-550, Jan. 2004.

[9] R. F. Hanssen, *Radar Interferometry. Data Interpretation and Error Analysis*. Dordrecht, The Netherlands: Kluwer, 2001.

[10] G. Schreider, Ed., *SAR Geocoding: Data and Systems*. Karlsruhe, Germany: Wichmann, 1993.

[11] H. A. Zebker and J. Villasenor, "Decorrelation in interferometric radar echoes," *IEEE Trans. Geosci. Remote Sens.*, vol. 30, no. 5, pp. 950–959, Sep. 1992.

[12] S. Williams, Y. Bock, and P. Pang, "Integrated satellite interferometry: Tropospheric noise, GPS estimates and implications for interferometric synthetic aperture radar products," *J. Geophys. Res.*, vol. 103, no. B11, pp. 27 051–27 067, 1998.

Daniele Perissin was born in Milan, Italy, in 1977. He received the master's degree in telecommunications engineering and the Ph.D. degree in information technology from the Politecnico di Milano, Milan, in 2002 and 2006, respectively.

He is currently working in the research group of Prof. F. Rocca and Prof. C. Prati at the Politecnico di Milano. His main research interest is in the field of SAR. Since 2002, he has been working on the permanent scatterers technique. He is the holder of a patent on the use of urban dihedral reflectors for combining multisensor SAR data.

Claudio Prati was born in Milan, Italy, on March 20, 1958. He received the laurea degree in electronic engineering and the Ph.D. degree from the Politecnico di Milano, Milan, in 1983 and 1987, respectively.

He is currently a Full Professor of telecommunications in the Dipartimento di Elettronica e Informazione, Politecnico di Milano. He is the holder of four patents on SAR image processing. He has published more than 100 papers on SAR data processing and interferometry. He is a Co-Founder of Tele-Rilevamento Europa, which is a remote sensing spinoff company of POLIMI.

Prof. Prati was awarded two prizes from the IEEE Geoscience and Remote Sensing Society (IGARSS'89 and IGARSS'99).

Marcus E. Engdahl was born in Finland. He received the M.S. degree in technical physics from the Helsinki University of Technology (HUT), Espoo, Finland, in 1996. He is an alumnus of the International Space University, Strasbourg, France.

From 1996 to 2003, he was a Research Scientist with the Laboratory of Space Technology, HUT. Since 2003, he has been an EO Applications Engineer in ESA-ESRIN, Frascati, Italy. In ESA, he has been responsible for coordinating R&D projects that deal with the observation of land and ocean surfaces with SAR, the development of SAR-related software toolboxes, and the organization of international workshops. His main research interests are in the land applications of SAR interferometry.

Mr. Engdahl was the main organizer of the Fringe 2005 Workshop held in Frascati, Italy.

Y. L. Desnos, photograph and biography not available at the time of publication.